Interaction of a mode-2 internal solitary wave with narrow isolated topography

David Deepwell,[1, a)] Marek Stastna,[1] Magda Carr,[2] and Peter A. Davies[3]

[1)] *Department of Applied Mathematics, University of Waterloo, Waterloo, Canada*

[2)] *School of Mathematics and Statistics, University of St. Andrews, St Andrews, UK*

[3)] *Department of Civil Engineering, University of Dundee, Dundee, UK*

(Dated: 27 June 2017)

Numerical and experimental studies of the transit of a mode-2 internal solitary wave over an isolated ridge are presented. All studies used a quasi-two-layer fluid with a pycnocline centred at the mid-depth. The wave amplitude and total fluid depth were both varied, while the topography remained fixed. The strength of the interaction between the internal solitary waves and the hill was found to be characterized by three regimes: weak, moderate, and strong interactions. The weak interaction exhibited negligible wave modulation and bottom surface stress. The moderate interaction generated weak and persistent vorticity in the lower layer, in addition to negligible wave modulation. The strong interaction clearly showed material from the trapped core of the mode-2 wave extracted in the form of a thin filament while generating a strong vortex at the hill. A criterion for the strength of the interaction was found by non-dimensionalizing the wave amplitude by the lower layer depth, a/ℓ. A passive tracer was used to measure the conditions for resuspension of boundary material due to the interaction. The speed and prevalence of cross boundary layer transport increased with a/ℓ.

[a)] ddeepwel@uwaterloo.ca

I. INTRODUCTION

Internal solitary waves (ISW) are a well-understood natural phenomena with a rich and extensive literature[1,2]. Much of the focus has been on waves of the first vertical mode, partly because the second vertical mode has only recently begun to be observed more frequently in the oceans[3–8]. These oceanic observations are often made on or near the coastal shelf[6,7], or in a region with a large sub-surface ridge[3–5]. Though all of the observations have been made in regions with dramatic variations in topography, nearly all of the related numerical and laboratory experiments that studied mode-2 waves to date have used a constant fluid depth.

Until now, the majority of both the physical and numerical literature on mode-2 waves has been devoted to mid-depth-centred waves with flat bottom boundaries[9–15]. These studies have expanded upon the original, weakly non-linear theory by Benjamin[16], and have described the characteristics of large amplitude mode-2 waves. Behavioural characteristics such as the wave speed, amplitude, and wavelength are now reasonably well understood for mode-2 waves within a constant fluid depth in the weakly non-linear to the strongly non-linear regime. The mass transport capabilities of such waves have also been discussed extensively in the literature[9,11,14,17]. Deepwell and Stastna[17] found that the transport efficiency has a strong dependence on Schmidt number, as well as the vertical profile of the pycnocline. Stratification parameters were found that reduced the effect of instabilities on the wave's trapped core, and enhanced its ability to transport material. Layers of unequal depth were studied in two recent papers[18,19]. Both articles found that even a small off-set of the pycnocline from the mid-depth led to significant asymmetry in the wave core, which in turn, contributed to an increase in instabilities therein. A strong off-set was also associated with the introduction of a mode-1 wavetrain trailing the mode-2 wave.

Recently, Terletska *et al.*[20] presented numerical simulations of mode-2 ISWs traveling over a step and showed that, depending on the size of the step, the incident mode-2 wave was either (i) unaffected, (ii) adjusted severely but re-formed as a smaller mode-2 wave or (iii) destroyed and created a mode-1 wave in the process. Mode-1 breather-like internal waves or mode-1 wavetrains were formed in all cases. In the weakly non-linear regime, Belogortsev, Rybak, and Serebryanyi[21] investigated the run-up of a mode-2 ISW onto a coastal shelf. Depending on the form and strength of the undisturbed stratification, the

initial convex mode-2 ISW either remained convex but was deformed, or was converted into a train of concave mode-2 ISWs.

We present here what we consider to be the first study that combines numerical and experimental descriptions of shoaling mode-2 ISWs. Rather than looking at the long term impact of shoaling on the wave, we focus on the interaction of the wave with the topography, specifically in terms of cross-boundary layer transport, vorticity generation and possible implications for sediment resuspension. In the context of the present numerical work, particle resuspension will be used to indicate the transport of a passive tracer out of the boundary layer and is therefore independent of the specific meaning used in sedimentology. In all numerical cases the passive tracer is already present in the simulation domain, and hence the Shields criterion or its many relatives are not relevant.

While the literature for shoaling mode-2 waves is now in its infancy, much can be learned from the shoaling mode-1 literature which has been predominantly concerned with waves traveling onto a shelf or slope (see Lamb and Xiao [22] and the references therein). Experiments on shoaling mode-1 ISWs indicate that such waves often pass through a critical point causing the wave to change polarity[23]. This often results in local overturning, vorticity generation, and heightened turbulent mixing. A few papers have discussed shoaling mode-1 ISW over a ridge[24–29]. Many of these have categorized the wave-hill interaction as either weak, moderate, or strong. Strong interaction has been associated with a change of polarity of the wave, causing breaking to occur and leading to strong vorticity generation and transport of near-bottom particles into the main water column[24]. It is this tracer resuspension that will be a central theme of this paper.

Though shoaling onto a shelf or slope is an important topic worthy of future study, we choose to investigate firstly mode-2 shoaling over an isolated ridge because of the associated ability to measure directly the impact that topography of a certain amplitude and slope will have on the evolution of the mode-2 ISW without the wave being completely destroyed. Many studies of shoaling mode-1 waves show heightened activity on the upstream side of the topography (Sveen *et al.* [24] for example). Using a ridge captures this wave-topography interaction while also investigating the long time behaviour of the wave once it has passed over the hill and returned to the original fluid depth.

The structure of this paper is as follows. Section II describes both the numerical and laboratory techniques and techniques used to create and characterize a mode-2 ISW. Section

III discusses the results of the interaction of the mode-2 ISW with the isolated ridge. Particular focus will be placed on the vortex dynamics. Section IV investigates the motion of the passive tracer originating at the bottom boundary. Section V explores the role of Reynolds number in tracer resuspension. Section VI outlines a criterion for categorizing the wave-hill interaction based upon the initial configuration. Finally, section VII will summarize the presented work.

II. METHODS

A. Experimental and numerical arrangement

We have followed the standard experimental procedure of creating ISWs by releasing an intermediate region into a background stratification. The background stratification was specified to have (or in the experiments, fit to) a hyperbolic tangent profile,

$$\bar{\rho}(z) = \rho_0 - \frac{\Delta\rho}{2}\tanh\left(\frac{z - L_z/2}{d}\right),$$

where $\Delta\rho$ and ρ_0 are the density difference between the top and bottom layers of the stratification and reference density respectively, d is the pycnocline half-width, and L_z is the total fluid depth. In this configuration the origin, $x = 0$ and $z = 0$, coincide with the upstream (left) end of the tank and the bottom of the tank, respectively (Figure 1).

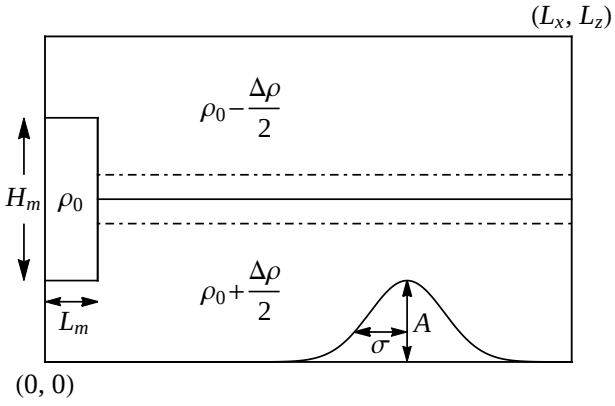

FIG. 1. Initial tank configuration (side view). Horizontal lines denote the location of the pycnocline centre (solid line), and pycnocline half-width (semi-dashed lines). The intermediate region with height H_m and width L_m contains density ρ_0 and is centred on the pycnocline (left end of tank).

A mode-2 ISW is formed by releasing an initially-confined, finite volume of fluid of intermediate density ρ_0 into this quiescent fluid system via a lock release mechanism. The vertical stratification profile of this intermediate region,

$$\bar{\rho}_m(z) = \rho_0 - \frac{\Delta\rho}{4}\left[\tanh\left(\frac{z-(L_z-H_m)/2}{d}\right) - \tanh\left(\frac{z-(L_z+H_m)/2}{d}\right)\right],$$

consists of three-layers. H_m and L_m are the height and width of the middle layer, respectively. The ratio of which, H_m/L_m, roughly sets the number of rank ordered mode-2 ISWs to be formed[30]. In the experiments a removable gate located at $x = L_m$ was used to separate the two regions. In the simulations a smooth weight function was used to transition between the two.

The domain for both the numerical and physical experiments was a long, narrow, rectangular channel with the dimensions given in Table I. All presented numerical simulations are two-dimensional. A couple of three-dimensional simulations were also completed but showed little difference from those in two dimensions. The fluid depth varied between 0.25 m and 0.40 m.

TABLE I. Tank dimensions and hill parameters.

Case	L_x (m)	L_y (m)	L_z (m)	A (m)	x_0 (m)	σ (m)
Num.	6.4	-	0.25-0.40	0.10	4.8	0.10
Exp.	6.4	0.4	0.30-0.40			

The isolated topography consisted of a single Gaussian hump,

$$h(x) = A\exp\left[-\left(x-x_0\right)^2/\sigma^2\right],$$

where A is the height of the hill, x_0 is the coordinate of the centre of the hill, and σ specifies the width of the hill. These hill parameters, given in Table I, remained unchanged for all simulations and experiments.

The aspect ratio, $A/\sigma = 1$, is large compared with typical topographical features in the ocean. Therefore we describe this hill as narrow. The maximum slope of 0.86 is steeper than the slope of 0.33 used in Sveen *et al.*[24] and Guo *et al.*[25], but is much smoother than the step function used by others[20,31,32]. Wave-hill interaction with broader topography will be discussed in a following article. Compared with the narrow topography of this article, a

longer wave-hill interaction time exists for a broad ridge resulting in greater deformation of the ISW.

Following the convention used in previous studies,[14,15,18] the characteristics describing a solitary mode-2 wave were calculated from the displacement of the $\rho(-L_z/2 \pm d)$ isopycnals from their original depth (Figure 2). The amplitude, a, is the average of the maximum displacement of these isopycnals, and the aft and fore wavelengths are the distance from the maximum isopycnal displacement to the half-maximum. The fore wavelength, λ_f, and the aft wavelength, λ_a, for the width ahead and behind the maximum amplitude, respectively. This asymmetry in the wave structure is caused by mixing and entraining of exterior fluid into the aft of the wave.

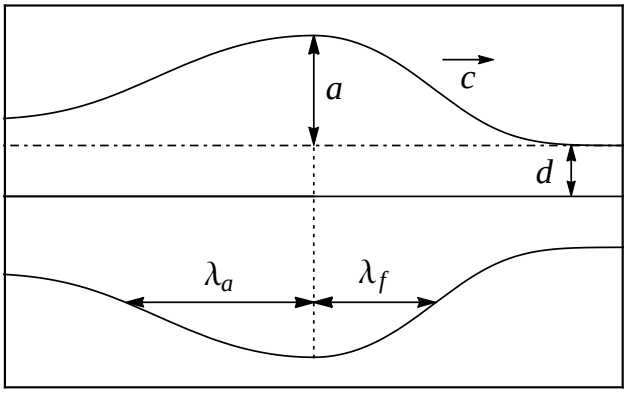

FIG. 2. Schematic of parameters for a rightward moving mode-2 ISW. Adapted from Deepwell and Stastna[17], with the permission of AIP Publishing.

Following past literature[14,15,18], we define the characteristic length as the pycnocline half-width, d. These articles used the mode-2 linear long wave speed[16],

$$c_0 = \frac{1}{2}\left(\frac{gd\Delta\rho}{\rho_0}\right)^{1/2},$$

for the velocity scale. However, since this scale is only applicable for small amplitude, linear waves we have we have used the average speed, c, of the wave between the time the wave settled after the lock release and before reaching the base of the topography. From this we define the Reynolds number as $\mathrm{Re} = cd/\nu$. The characteristic time is defined in terms of the pycnocline half-width and this velocity scale, $T = d/c$. This then defines the non-dimensional time, $\tilde{t} = t/T$.

The parameters of the numerical simulations and experiments are listed in Table II. In summary, the fluid depth varied between 0.25 m and 0.40 m, and the intermediate fluid

TABLE II. Numerical and experimental parameters.

Case	L_z (m)	L_m (m)	H_m (m)	d (mm)	$\Delta\rho/\rho_0$	c/c_0	a/d	Sc	Re	Interaction
Numerical										
2504	0.25	0.3	0.04	10	0.023	1.37	0.69	10	163	M
2506	0.25	0.3	0.06	10	0.023	1.70	1.47	10	202	S
2508	0.25	0.3	0.08	10	0.023	1.94	2.24	10	230	S
3002	0.30	0.3	0.02	10	0.023	1.12	0.21	10	133	W
3004	0.30	0.3	0.04	10	0.023	1.40	0.75	10	167	W
3006	0.30	0.3	0.06	10	0.023	1.75	1.55	10	207	M
3007	0.30	0.3	0.07	10	0.023	1.89	1.96	10	224	M
3008	0.30	0.3	0.08	10	0.023	2.00	2.33	10	237	M
3009	0.30	0.3	0.09	10	0.023	2.10	2.70	10	249	S
3010	0.30	0.3	0.10	10	0.023	2.17	3.04	10	257	S
3012	0.30	0.3	0.12	10	0.023	2.24	3.48	10	265	S
3506	0.35	0.3	0.06	10	0.023	1.78	1.61	10	211	W
3508	0.35	0.3	0.08	10	0.023	2.05	2.41	10	243	M
3509	0.35	0.3	0.09	10	0.023	2.15	2.79	10	255	M
3510	0.35	0.3	0.10	10	0.023	2.21	3.08	10	263	M
3512	0.35	0.3	0.12	10	0.023	2.29	3.43	10	272	S
4008	0.40	0.3	0.08	10	0.023	2.07	2.45	10	246	W
4010	0.40	0.3	0.10	10	0.023	2.26	3.14	10	268	M
4012	0.40	0.3	0.12	10	0.023	2.36	3.56	10	280	M
Experimental										
110516	0.300	0.3	0.061	8.1	0.021	2.04	2.06	-	339	W
060516	0.300	0.3	0.086	7.2	0.024	2.35	3.42	-	348	S
290416	0.301	0.3	0.111	9.0	0.023	2.11	3.20	-	428	S
260416	0.355	0.3	0.085	9.5	0.018	2.10	2.78	-	410	M
020516	0.356	0.3	0.110	9.5	0.022	2.13	3.13	-	456	M
090516	0.400	0.3	0.096	10.4	0.021	2.07	2.78	-	497	W
040516	0.400	0.3	0.140	10.4	0.022	2.26	3.46	-	555	M

depth varied between 0.02 m and 0.12 m. Within the simulations, the non-dimensionalized density difference was 2.3% a value which matches well the density differences used in the laboratory experiments. The Schmidt number, $\mathrm{Sc} = \nu/\kappa$, was fixed at 10 for all primary simulations. The effect of adjusting Schmidt number and Reynolds number will be looked at in section V.

The interaction can be categorized broadly into three main regimes, designated here as weak (W), moderate (M), or strong (S) interaction. The strong interaction exhibits a clear loss of material from the mode-2 wave core and strong separation of the bottom boundary layer (BBL). The moderate interaction is characterized by the creation of a persistent vortex at the hill crest, while the wave is slightly adjusted. The weak interaction leaves the mode-2 ISW essentially unaffected by the transit. These categories are comparable with those introduced by Sveen *et al.*[24] in the case of a mode-1 wave of depression, where the interaction with ridge topography was classified empirically as either wave breaking, moderate, or weak.

B. Numerical methods

The governing equations are the Navier-Stokes equations under the Boussinesq approximation,[33]

$$\begin{aligned}
\frac{D\vec{u}}{Dt} &= -\frac{1}{\rho_0}\nabla p + \frac{\rho}{\rho_0}\vec{g} + \nu\nabla^2\vec{u}, \\
\nabla\cdot\vec{u} &= 0, \\
\frac{D\rho}{Dt} &= \kappa\nabla^2\rho, \\
\frac{DT}{Dt} &= \kappa_T\nabla^2 T,
\end{aligned}$$

where $\vec{u}$ is the velocity, T is a passive scalar field, p is the pressure, $\vec{g}$ is the gravitational acceleration, ν is the kinematic viscosity, $\frac{D}{Dt} = \frac{\partial}{\partial t} + \vec{u}\cdot\nabla$ is the material derivative, κ and κ_T are the molecular diffusivity of the density and tracer, respectively, and ρ and ρ_0 are the density and reference density, respectively. Though the Navier-Stokes equations are written in dimensional form, the presented density fields will be non-dimensionalized as the density anomaly, $\tilde{\rho} = (\rho - \rho_0)/\rho_0$.

To simulate the formation and progression of a mode-2 ISW we have used the Spectral Parallel Incompressible Navier-Stokes Solver (SPINS), details of the construction and validation of which are described in Subich, Lamb, and Stastna[34]. No slip boundary conditions

were used in the vertical (top and bottom boundaries) through the use of Chebyshev grids to cluster points within the boundary layer. The free slip condition was used in horizontal directions by using Fourier grids. The grid resolution is listed in Table III. Time dependent simulations were completed on the high-performance computer cluster SHARCNET (www.sharcnet.ca).

TABLE III. Numerical resolution.

N_x	N_z	Δx (mm)	$\Delta z_{\max}$ (mm)
4096	384	1.56	1.23

We have checked for numerical convergence by conducting grid coarsening studies. As this is a spectral method we require only the number of grid cells equivalent to the wavenumber associated with a particular feature. If this is not the case, sharp gradients may not be handled adequately by the spectral method and can cause unphysical growth of a field. In particular, this can occur in the density field. In addition to the grid coarsening studies, we have checked to make sure that the density field does not increase above its initial maximum, and below its initial minimum.

C. Laboratory procedure and measurement technique

The stratification was formed by slowly dripping a layer of less dense fluid on top of a more dense layer through an array of sponges. The two layers were both composed of miscible homogeneous brine solution, with the bottom and top layers having typical densities of $\rho_3 = 1047 \pm 2$ kg/m^3 and $\rho_1 = 1025 \pm 2$ kg/m^3, respectively. As a result of the miscibility of salt, the two layers diffused to form a continuous stratification that approximates closely the hyperbolic tangent profile used in the numerical model simulations.

After the lower layer in the main section of the tank had been filled, the gate was installed and fully closed. The main section of the tank was then stratified and at the same time, fluid of density ρ_3 was added behind the gate to maintain equilibrium pressure between the two sides of the gate. After the stratification was formed in the main section of the tank, a small valve located on the bottom of the channel was used to lower the level of the fluid behind the gate. The fluid was dropped by an amount equal to the depth required for the wave-generating volume of mixed fluid, of density $\rho_2 = (\rho_1 + \rho_3)/2$. The mixed fluid was

added using a floating sponge and a top layer of density ρ_1 was added subsequently through the same sponge. The fluid behind the gate was lowered and filled until the top and bottom layers behind the gate contained equal volumes. The resulting stratification then resembled that of Figure 1, with the addition of the gate a distance of L_m away from the left (upstream) wall.

The form of the stratification was measured using high precision, micro-conductivity sensors[35] connected to a rigid rack and pinion traverse system fitted with a potentiometer. Density profiles were obtained by traversing the sensors vertically through the water column and then calibrating the potentiometer output and conductivity data against known values of distance and fluid density. The sensors were used to ensure that the mid-depth of the mixed layer behind the gate coincided with the mid-depth of the pycnocline in the main section of the tank.

Upon removal of the gate, the motion of the resultant mode-2 ISW was captured on three digital video cameras that were set up outside of the tank, viewing from the side. The cameras were centered, in the vertical direction, on the pycnocline in order to minimize distortion and perspective errors in this portion of the flow field. The middle camera was centered, in the horizontal direction, on the apex of the topography. The cameras were arranged to have overlapping fields of view and their operation was synchronized in time.. Neutrally-buoyant, light-reflecting tracer particles of diameter $100 - 300$ μm, were used to seed the water column. An array of light boxes placed below the transparent base of the tank generated a continuous, narrow, collimated light sheet which illuminated a vertical section in the mid-plane of the tank. The motion of the tracer particles within the light sheet were viewed and recorded from the side by the three cameras. A rigid lid was placed on top of the water column to aid comparison with the numerical simulations and to minimize surface disturbances and evaporation.

The software package *DigiFlow*[36] was used to process the digital video records. The time series function of *DigiFlow* was used to measure wave speed and wave velocity while the Particle Image Velocimetry (PIV) function was used to calculate continuous synoptic velocity and vorticity field data along the illuminated cross-section in the middle of the tank. Further details on these techniques can be found in Carr, Davies, and Hoebers[18].

III. RESULTS: WAVE-HILL INTERACTION

Here we present the results of a solitary mode-2 internal wave interacting with a narrow topography. We investigate the adjustment of the mode-2 ISW due to the hill, and the vorticity generation within the lower layer.

The wave speed is modulated through its non-linear dependance on wave amplitude. By increasing the amplitude, and therefore, the wave speed (all other parameters remaining fixed), the flow changes from one in which negligible interaction is detected to one in which there is moderate vorticity roll-up until, finally, at large amplitude, strong vortex generation is observed. In this work we have fixed the width of the collapse region, L_m, while using the height, H_m, to vary the amplitude.

A. Weak interaction

When the interaction is weak (see Table II for the relevant cases), the wave passes over the hill mostly unchanged. The wave speed and amplitude are perturbed by approximately one to two percent of their pre-interaction values. However, these changes are on the order of the losses due to the natural deceleration and core leakage associated with large amplitude mode-2 waves. As the wave travels over the hill, the local surface stress along the bottom boundary increases from the pre-hill value because of the increase in flow speed in the lower layer due a reduction in depth. In the numerical simulations this shear created a weak, $\mathcal{O}\left(0.5\ \mathrm{s}^{-1}\right)$, vorticity field above the hill. In the experimental cases it was far more difficult to measure the vorticity field due to its weak nature, but some particles where clearly seen to be lifted off from the hill surface.

B. Moderate interaction

A moderate wave-hill interaction experiences the removal of a small amount of fluid from the lower half of the mode-2 wave which causes slight density over-turning to occur (Figure 3a and c)[37]. This small overturn is associated with the generation of two horizontal patches of vorticity within the pycnocline (Figure 3d and f) which continue to impact the BBL because of the close proximity to the hill crest. The obstruction of the mode-2 wave also leads to boundary layer separation along the hill and the roll-up of a single vortex (Figure

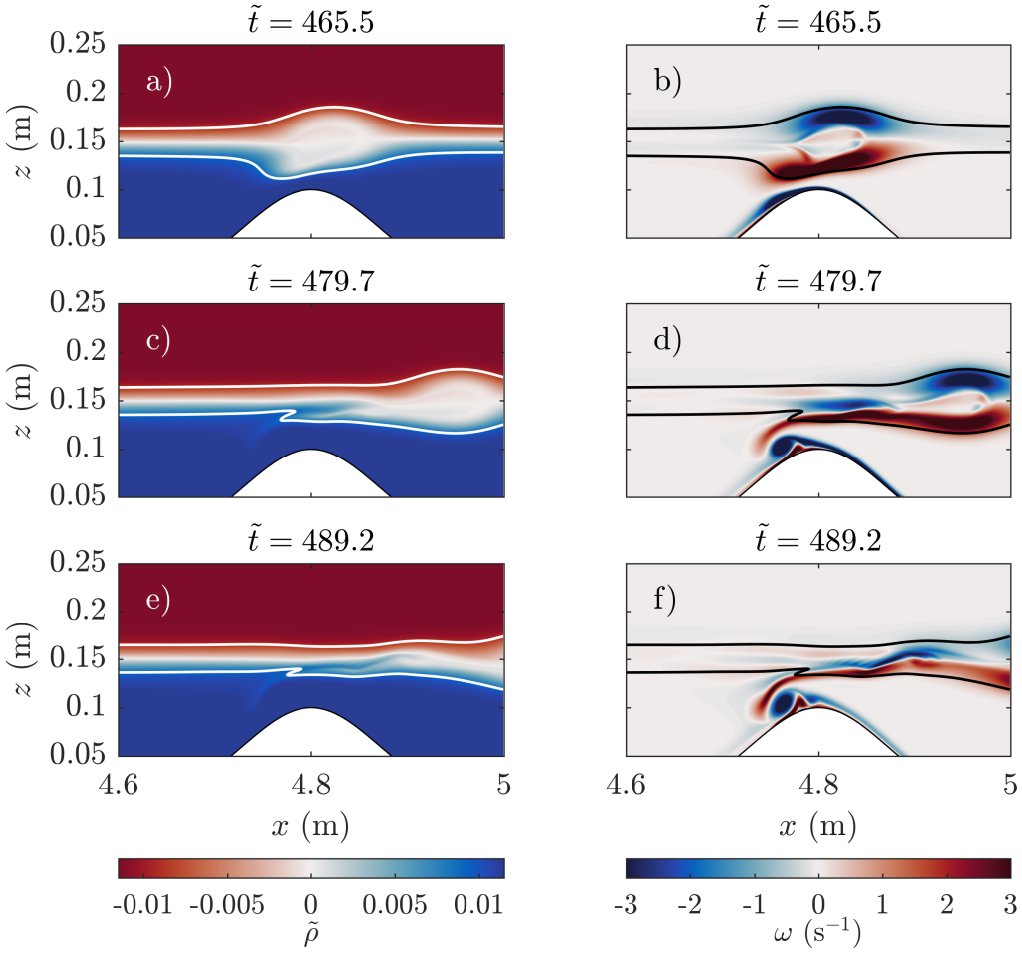

FIG. 3. Density anomaly (a,c,e) and vorticity (b,d,f) for a moderate interaction (numerical case 3008). White (black) contours in left (right) column are the characteristic isopycnals.

3d and f) . As a result of this vortex generation, some fluid is pulled from the pycnocline into the boundary layer. This boundary layer separation occurs after the wave passes the crest of the hill in a process similar to the vorticity roll-up discussed in Harnanan, Soontiens, and Stastna[38] and Olsthoorn and Stastna[39].

The traversal of the wave over the hill creates a vortex located just above and upstream of the hill peak. This vortex moves towards the hill peak where separation occurs because of a favourable change in topography. Figure 4 shows the false colour image of this separation (left column) and the vorticity (right column) from the experimental case 040516. Figure 4a and c show the particles used in the PIV measurement and the topography (bright, yellow, arcing curve, and attached perpendicular spokes used in construction). The first row of Figure 4 are 7.8 non-dimensional time units (1.5 s) after the onset of separation. 6.5

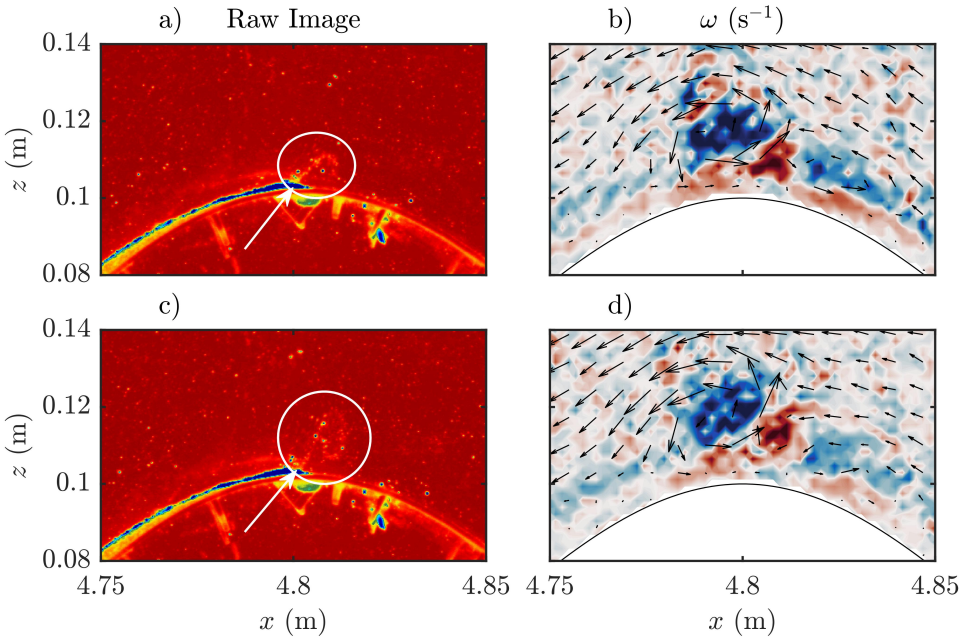

FIG. 4. False colour of the raw image (a,c) and vorticity (b,d) for moderate vorticity roll-up (experimental case 040516). (a,b) 34.7 non-dimensional time units (6.7 s) after the wave crossed directly over the hill peak, (c,d) 6.5 non-dimensional time units (1.25 s) later. In the left column, the circle emphasizes the resuspended particles and the arrow points to the separation point. The vorticity colour scale is the same as the right column of Figure 3.

non-dimensional time units (1.25 s) later the separation continues and particles from the boundary layer were advected vertically into the water column (Figure 4c). These particles remain suspended for the remainder of the experiment and gradually disperse over the lower layer. The vorticity (Figure 4b and d) matches the results from the numerical simulations (right column of Figure 3), and reveals that the slow vortex is the driving force for the separation and particle resuspension.

The vortex remains atop the hill well after the wave has passed. Thus, the instabilities produced by one wave may interact with a subsequent ISW resulting in amplified transport of BBL material into the water column. This interaction is seen when the next rank-ordered mode-2 ISW reaches the hill (Figure 5). The second interaction briefly increases the vorticity but causes the vortex to lose some spatial structure which accelerates its collapse.

Since some induced vorticity remains (and is stronger with larger wave amplitude) when the second wave passes over the hill, we can use this time as a lower bound on the permanence

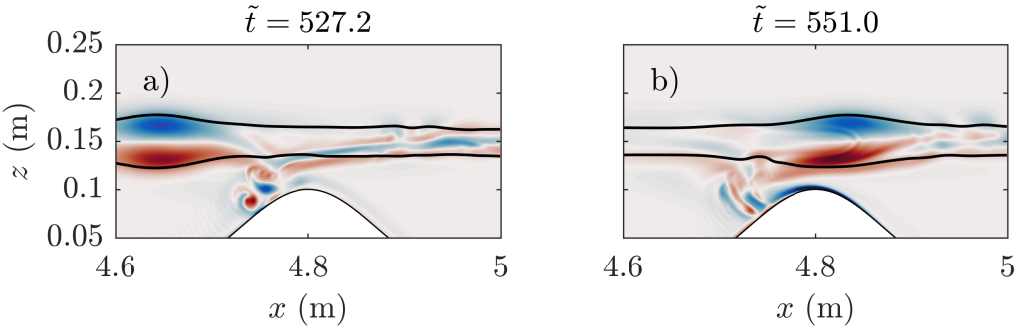

FIG. 5. Vorticity of the second mode-2 ISW for moderate interaction (numerical case 3008). The colour scale is the same as the right column of Figure 3.

time of that vorticity. For both numerical and experimental interactions of moderate size this is $\mathcal{O}(50)$ non-dimensional time units. In the South China Sea, Ramp *et al.*[4] found a train of mode-2 ISWs with wave arrival times in the range of 2-20 non-dimensional time units which indicates that it is likely that induced motions from one interaction will impact a subsequent one. For a typical train of 4-5 ISWs this could have significant implications for a near-bottom ecosystem.

The moderate interaction is characterized by minimal mixing in the pycnocline (the pycnocline grew in width by a couple millimetres) coupled with delayed vorticity roll-up near the peak of the hill. This indicates that while there is but a small perturbation to the wave, significant vorticity is still produced at the bottom boundary which is capable of transporting material from the hill surface into the water column. The majority of the vortex roll-up forms while the wave is on the lee side of the hill, and remains long after the wave has passed.

Though not shown, the moderate interaction also exhibits the creation of small amplitude mode-1 waves ahead of and behind the mode-2 ISW. The sudden reduction in fluid depth causes the ISW to be deflected vertically, causing a break in symmetry across the pycnocline. Since the ridge is narrow, the mode-2 ISW soon returns to its equilibrium depth where it re-stabilizes. The trailing wavetrain consists of 3-4 waves with an amplitude and wavelength of approximately 1 cm and 10 cm, respectively. These trailing waves, however, are not phase locked with the mode-2 ISW and eventually disperse behind the wave. The leading mode-1 ISW of depression has an amplitude and wavelength of approximately 5 mm and 30 cm, respectively. It was difficult to notice evidence of the leading wave in the experimental cases,

while the trailing waves were easily identified.

Despite the large size of the hill, the wave still remains coherent throughout the entire transit over the topography. The criterion for wave breaking will be discussed below, but it is clear that a large amplitude wave may travel largely unmodulated even with steep topography. Case 4010 (not shown) is a prime example as the wave amplitude in this case is quite large, but only modest vorticity roll-up is observed. This has important implications to regions with multiple ridges since waves may traverse each with minimal modification in shape, yet still impact the BBL.

C. Strong interaction

Strong wave-hill interaction occurs when the wave amplitude is large enough to cause core material to nearly impact the crest of the hill. Unlike the moderate interaction, an unmistakable filament of fluid is extracted from the mode-2 wave by the blocking of the hill (Figure 6c). It is this defining feature that is used to distinguish between moderate and strong interactions. This strong density over-turning quickly equilibrates (Figure 6e) while causing a sudden increase in viscous dissipation and mixing along the pycnocline (the pycnocline width grew by approximately 5 mm).

The formation of the filament leads to the formation of a asymmetric vortex dipole. The counterclockwise vortex is much stronger and travels nearly perpendicularly away from the hill (Figure 6d). This vortex is quite energetic and moved from the boundary layer into the pycnocline. It is expressly clear that in interactions of this type, fluid from the boundary layer and pycnocline are brought in contact, allowing them to be mixed. Therefore, this process may be efficient at lifting and dispersing material originating in the boundary layer into the water column.

The filamentary extraction realized in this large amplitude case has been described before in the case of a mode-1 ISW when traveling over a step[31] and over a ridge[24]. Though the waves considered in these studies were mode-1, the density fields appear quite similar in the lower layer (see Figure 15c from Maderich *et al.*[31] and Figure 7c from Sveen *et al.*[24]). Looking back at Figure 6, it is clear that the upper portion of the mode-2 ISW is essentially unaffected by the interaction with the bottom topography. All the kinetic energy induced by the interaction is isolated in the lower layer. This indicates that the dynamics of the

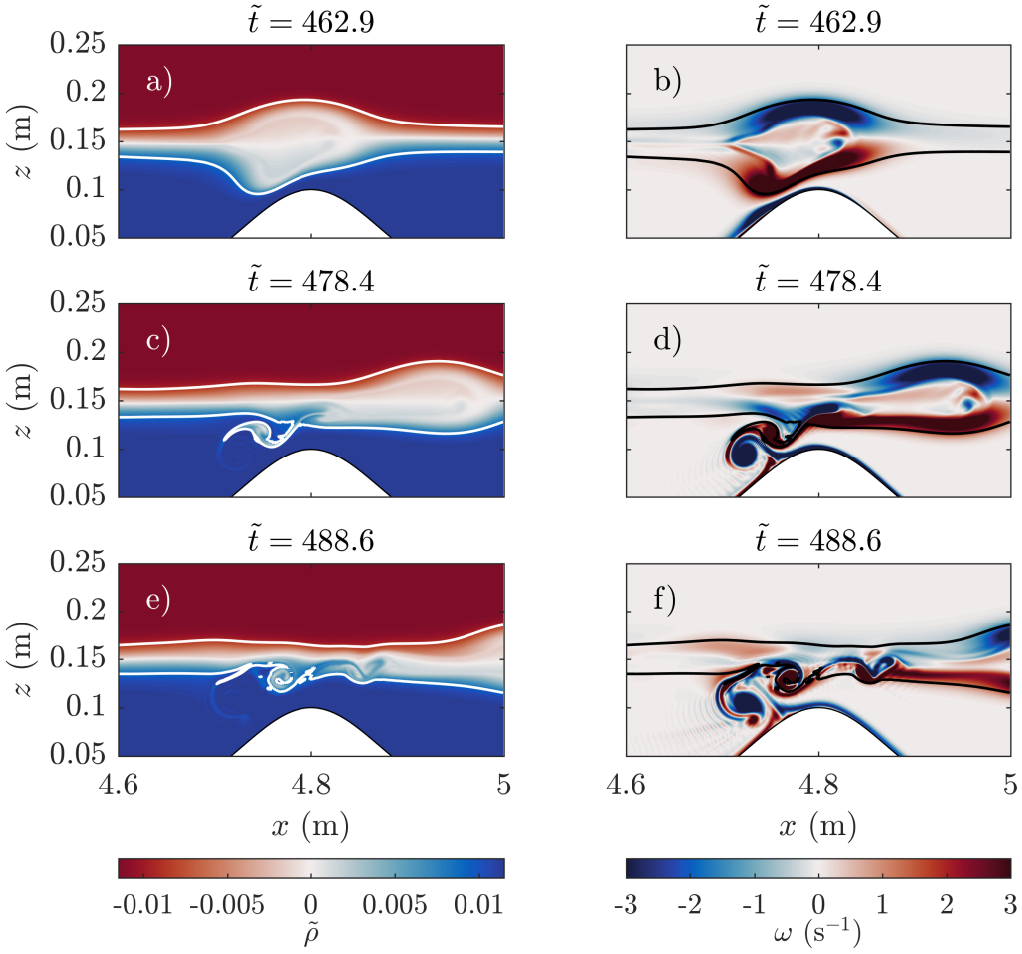

FIG. 6. Density anomaly (a,c,e) and vorticity (b,d,f) for the strong interaction (numerical case 3010). All other contours are the same as in Figure 3.

interaction are independent of the wave mode number.

Though not shown, trailing and leading mode-1 waves are again generated by the interaction with the hill in the strong interaction cases. The trailing wavetrain, however, is weaker than that formed in the moderate interaction because of the more chaotic interaction. The leading mode-1 ISW was of comparable amplitude and wavelength to that formed in the moderate case. More noticeably, the mode-2 ISW is smaller after the interaction because of the loss of core material - approximately 24% based on the product of the amplitude and wavelengths, $a(\lambda_a + \lambda_f)$.

Thus far, the interesting wave-hill interactions have been described as either moderate or strong. The laboratory experiments, however, demonstrated another state that was a combination of the two. This interaction is characterized by the generation of strong

vorticity in the lower aft of the wave but does not result in the formation of a thin element as in the strong interactions. For clarity, we will call the interaction that forms a filament a filamentary extraction (FE), while the interaction with similar vorticity but no filament will be called a globular extraction (GE). For the purpose of categorizing the GE interaction, it is listed as a strong interaction because of the similarities in the dynamics of the two.

Figure 7 compares these two interaction types (see supplementary material for video photage). The left column shows the globular extraction, while the right shows the filamentary extraction. Both types of interactions exhibit a similar waveform when directly over the hill (Figure 7a and b), but have different extraction mechanisms. Six non-dimensional time units later the two waves show different behaviour. The FE interaction displays a long,

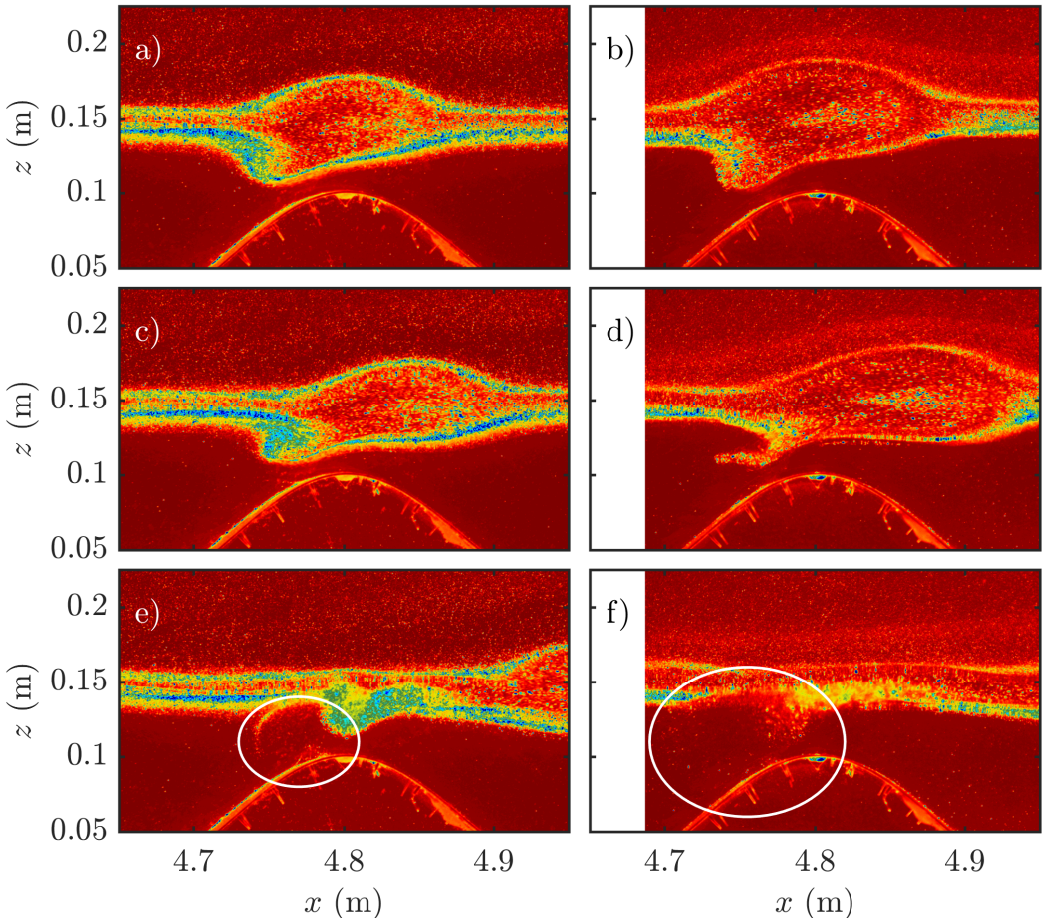

FIG. 7. False colour time series of the raw image for the mass extraction of type: (a,c,e) globular extraction (experimental case 060516) and (b,d,f) filamentary extraction (experimental case 290416). (c,d) and (e,f) are 6 and 23 non-dimensional time units after (a,b), respectively.

thin 'finger' of material emanating from the wave core (Figure 7d), while the GE interaction shows a large vortex of core material in contact with the pycnocline (Figure 7c). In the lower layer, the induced turbulence is comparable between the two cases, but covers different areas (Figure 7e and 7f).

The turbulent area is greater in the FE case compared to the GE case (circled region of Figure 7e and 7f). The filamentary case is forced into a far more unstable situation, but the amount of mass is not as large as in the globular case. Instead, the globular case has more core fluid transported to lie below its equilibrium depth. This caused similar reductions in the lower layer depth which increased the surface shear along the hill and the formation of vorticity.

The filamentary and globular extraction types are similar. Filamentary extraction simply has the required energy to move core fluid deep enough to form the filament. Since the absolute wave speeds are similar between the two cases we surmise that the additional energy for the filamentary extraction came from the larger absolute ISW amplitude. The larger amplitude would force the return flow to exist within the narrower region between the wave and the hill, thereby increasing the shear.

The vorticity fields from the PIV measurements for the globular and filamentary extraction types are similar (Figure 8) and match that from the filamentary extraction type from simulations (Figure 6b). Vorticity calculations derived from the PIV data after the fluid has become three-dimensional are unreliable as particles are no longer moving predominantly in the x-z plane. As the flow becomes three-dimensional, particles may pass through the illuminated plane making it nearly impossible to track a specific particle.

It should be mentioned that the globular extraction type was not seen explicitly within the numerical simulations. There are instances of removal of material from the core in a globular-like fashion, but these occur generally in smaller quantities than those seen in Figure 7c. This difference can be attributed to the presence of spurious external factors in the experiments compared with a simulation (e.g. artifacts associated with the lock release mechanism, the effects of sidewalls, and the effects of a surface that is free over a portion of the experimental flume).

In both the moderate and strong wave-hill interactions a long-wave mode-1 wavetrain is formed behind the mode-2 ISW. This matches the numerical simulations, but, unlike the simulations, the experiments do not show the formation of a leading mode-1 ISW. This is

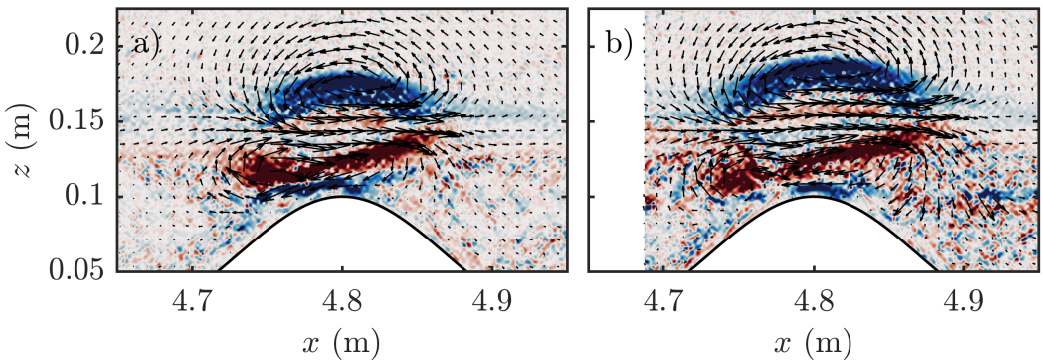

FIG. 8. Vorticity and velocity vector field for (a,c,e) globular extraction (experimental case 060516) and (b,d,f) filamentary extraction (experimental case 290416) at the moment the wave is directly above the hill crest. The colour scale is the same as the right column of Figure 3.

likely due to the leading wave having such a small amplitude that it was not perceptible from the PIV data.

D. Summary

In spite of the large asymmetry in layer depth caused by the topography, the mode-2 wave did not deform in such a way as to significantly radiate mode-1 waves. While some mode-1 waves are radiated, their amplitudes are small, $\mathcal{O}$ (1 cm) at the largest. Aside from the strong wave-hill interactions, the wave amplitude, wavelength and speed of the transmitted mode-2 wave are all comparable to their values prior to interacting with the hill. In Case 3012 (a strong interaction example which experienced strong adjustment of the mode-2 wave), the amplitude, wavelength and wave speed were reduced by approximately 18%, 14% and 5%, respectively. The interaction time is short, $\mathcal{O}$ (30) non-dimensional time units, such that the work done on the wave by the hill is minimal. Comparisons to wave-hill interaction in the case of a broad hill with a longer interaction time will be made in a follow-up article, which will discuss further the formation of mode-1 waves.

IV. CROSS BOUNDARY LAYER TRANSPORT DUE TO VORTICITY GENERATION

A standard quantity used to assess the likelihood of particle resuspension is the surface stress. The surface stress along the hill was calculated from the stress vector, $f_i = \tau_{ij} n_j$[33], where τ_{ij} is the Cauchy stress tensor and n_j is the unit normal to the surface of the hill. For two-dimensional simulations, the component tangential to the surface can be explicitly written as

$$f_s(x) = \frac{\mu}{1 + h'(x)^2} \left(2h'(x) \left(w_z - u_x \right) + \left(1 - h'(x)^2 \right) \left(u_z + w_x \right) \right),$$

where subscripts and primes on the right hand side denote differentiation with respect to the given variable. The total, absolute tangential surface stress,

$$f_{\text{tot}} = \int_0^{L_x} |f_s(x)| \sqrt{1 + h'(x)^2} dx,$$

indicates the overall strength of the wave-hill interaction.

The computed time history of the surface stress for fluid depth of 30 cm (Figure 9) indicates clearly that the wave-hill interaction occurred at $\tilde{t} \approx 465$. Comparing Figures 3 and Figures 6 to Figure 9 it is clear that the maximal surface stress is associated with the obstruction of core material. In the strong interaction case (Figure 6a and c) this occurs just prior to the formation of the filament.

Figure 9 demonstrates that, prior to the wave-hill interaction, the total surface stress is relatively constant with time once the wave has formed and become stable. In all cases, the surface stress at least doubles from the pre-interaction value while, in a couple of cases, ($H_m = 0.08$ m and $H_m = 0.09$ m) the value reaches almost triple the pre-interaction stress. After the interaction, the stress remains above the pre-interaction value due to the prevalence of the vorticity above the hill. Some cases show the interaction of the second rank-ordered mode-2 wave at approximately $\tilde{t} = 540$.

As fluid depth increases, the required amplitude for separation increases due to a reduction in bottom surface stress. On an oceanic scale this indicates that resuspension occurs when the wave is large, the pycnocline is close to the hill crest, or a combination of the two. A proper criterion for separation and the formation of the filamentary extraction process is presented in Section VI.

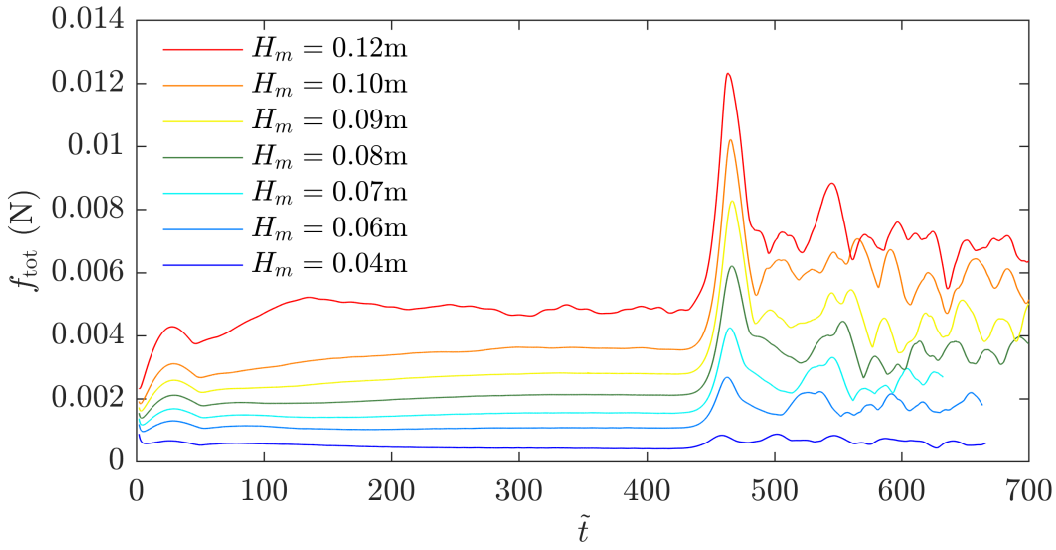

FIG. 9. Variation of total bottom surface stress, f_{tot}, with non-dimensional time, $\tilde{t}$, for fluid depth $L_z = 0.30$ m and H_m values shown (numerical cases 3004 - 3012).

Further investigation of the role of surface stress and vorticity was done with the addition of a passive tracer localized to within one centimetre above the bottom topography. So far, it has already been seen that vorticity is easily produced on the upstream side of the hill, and that sufficient surface stress exists to cause separation.

In the moderate and strong interaction cases, vorticity produced on the upstream side of the hill acted to lift part of the tracer away from the hill (Figure 10). The majority of the tracer movement was confined within the vortex on the side of the hill on which the wave originates. In the moderate interaction (left column of Figure 10) the vorticity remains coherent and persistent long enough to move the tracer away from the bottom surface. The strong interaction is sufficiently energetic to transport material rapidly from the BBL to the edge of the pycnocline (Figure 10d). In both interactions, it is the coherent vortex which is the primary driver for the transport of the tracer. The strength of the vortex is weaker in the moderate interaction, and therefore the cross boundary layer transport is considerably slower. In all interaction types the vortex was unable to penetrate the pycnocline causing all the resuspended material to remain within the lower layer.

In either interaction case, the tracer remains suspended long after the interaction of the initial mode-2 ISW with the hill (Figure 11). At $\tilde{t} \approx 710$, the first four rank ordered mode-2 ISWs have all travelled over the hill. The resuspended tracer from each interaction has been

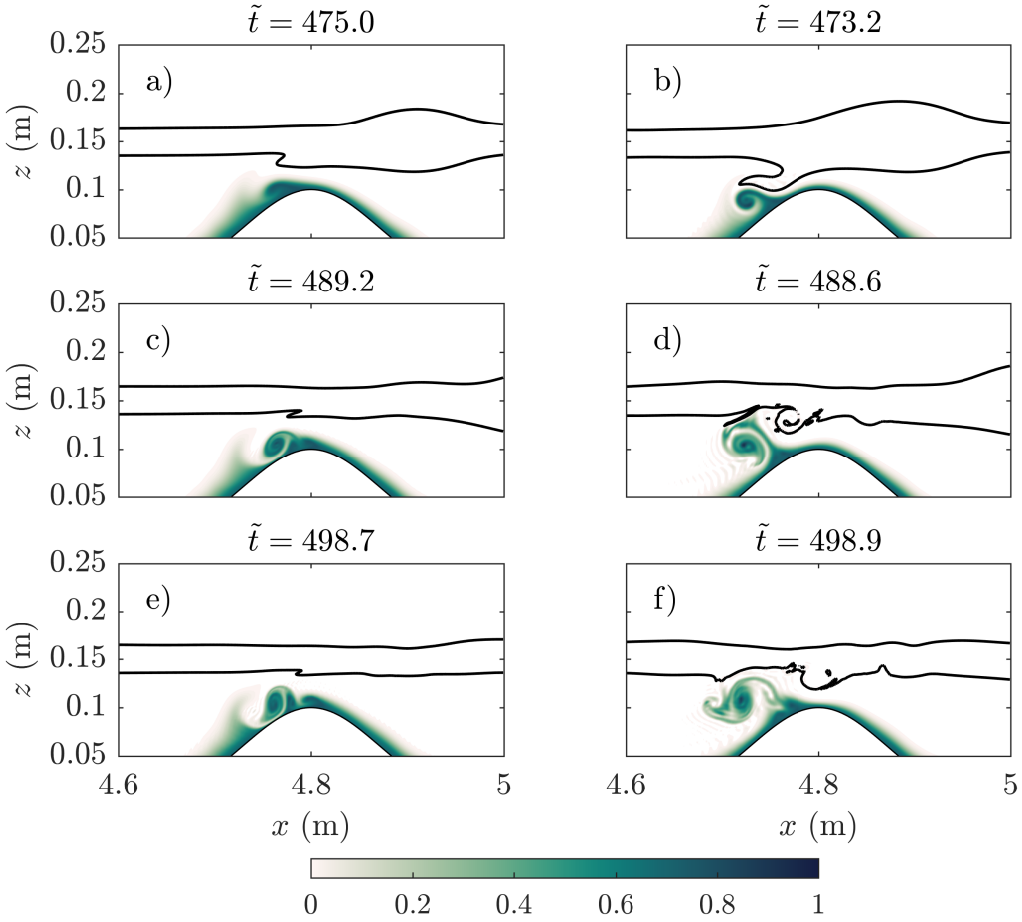

FIG. 10. Passive tracer for (a,c,e) moderate (numerical case 3008) and (b,d,f) strong (numerical case 3010) interaction.

advected away from the hill in the direction opposite to that of the wave. Should there be fixed mode-2 generation sites (as proposed by Ramp *et al.*[4] for the Heng-Chun ridge) then particulates will be directed preferentially towards those generation sites.

Figure 11 reveals that within a given time-frame, stronger wave-hill interactions (right column) resuspend more BBL material over a wider area than for a moderate interaction (left column). Less BBL material was resuspended at an increased fluid depth (second row) due to the weaker surface stress. Though not plotted, there is a non-negligible amount of tracer transported in weak interactions as well. The ease to which bottom boundary layer material is resuspended is clear and should not be neglected. A possible feature to include in future work is a negatively-buoyant tracer with a settling velocity. Herein, we have been concerned with the resuspension capabilities of the wave-hill interaction, and the neutrally

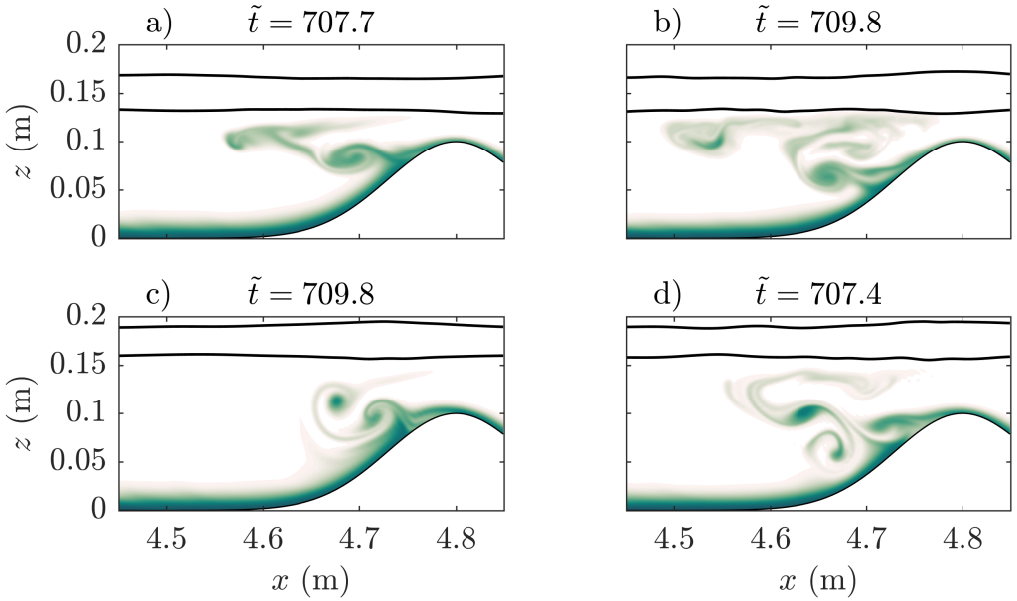

FIG. 11. Passive tracer well after the transit of the mode-2 ISW for numerical case a) 3008 and b) 3010 c) 3510 d) 3512. Moderate (strong) interaction corresponds to the left (right) column. The colour scale is the same as Figure 10.

buoyant tracer is ideal for this purpose.

Breaking waves were easily distinguished from their non-breaking counterparts by the degree of extraction of core material from the mode-2 ISW. They are an interesting dynamical effect which suspends BBL material rapidly by means of vorticity generation at the hill crest. The moderate interactions experienced a calmer vorticity roll-up which still moved substantial BBL material. Therefore, mode-2 waves are an efficient means of both moving BBL material along the topography and resuspending particulates.

V. REYNOLDS NUMBER INFLUENCE

Now that the cross boundary layer transport of the tracer has been discussed, we investigate the impact of changing the Schmidt and Reynolds numbers on a specific case. Numerical simulations are a particularly useful tool for this type of study, compared with laboratory experiments. Since case 3010 most clearly shows the filamentary extraction (Figure 6) and the quickest response to the interaction with the hill, it is on this case that we will focus.

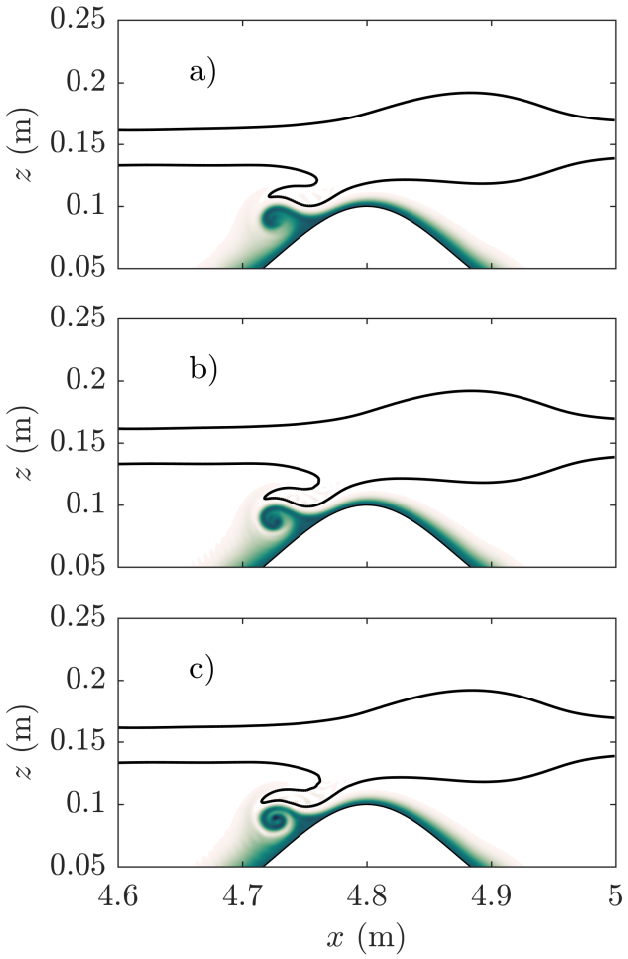

FIG. 12. Passive tracer for strong interaction (numerical case 3010) at $\tilde{t} = 473.2$ with a) Re = 129, b) Re = 257, and c) Re = 514. The colour scale is the same as Figure 10.

Case 3010 was restarted just prior to interacting with the hill ($\tilde{t} = 452.6$). In each new restart, either the density diffusivity, the viscosity, or both were halved or doubled. This created a parameter sweep where either the Reynolds number was held fixed while the Schmidt number varied, the converse, or where both varied.

Figure 12 shows the tracer for varying Reynolds number and a fixed value of Sc = 10. This parameter sweep was chosen for presentation as it had the most variation in the tracer field. In contrast, a varying Schmidt number with fixed Reynolds number had no noticeable impact on the observed distribution of the tracer. The density field (contours in Figure 12) was found to be comparable for all Reynolds numbers used. The tracer field shows similar dynamical behaviour in each case; chiefly, the formation of a vortex which acts to resuspend

the tracer. However, the visible details within that vortex structure increase with increasing Reynolds number.

As we are primarily focused on the resuspension efficiency of the wave-hill interaction, it is evident that the Reynolds number does not have a primary role in the shear produced for the range reported. It should be noted that the Reynolds number for mode-2 waves shoaling in the field[6] are expected to be $\mathcal{O}(10^5)$, and hence it is possible that finer scale structure, or even secondary instabilities could be observed.

VI. WAVE BREAKING CRITERION

A criterion for wave breaking can be formulated in terms of the primary determining parameters for the interaction, namely the wave amplitude, fluid depth, pycnocline width, and topography amplitude. The non-dimensional amplitude, a/ℓ, where $\ell = L_z/2 - d - A$ is the depth of the lower layer at the hill crest, provides the proper scaling of the wave amplitude relative to the minimum lower layer depth. Figure 13 shows the interaction types for given non-dimensional wave amplitude (as defined above) and wave speed. For $a/\ell < 1/3$ the wave-hill interaction is weak (W), while $a/\ell > 1/2$ manifests the strong FE interaction (S) which is a clear sign of wave breaking. For $1/3 < a/\ell < 1/2$ the interaction is moderate (M) and exhibits the vorticity roll-up interaction.

One case described as a moderate interaction has $a/\ell > 0.5$. This case is very nearly a strong interaction as it shows the beginning formation of the filament being extracted from the ISW core. Nevertheless, because the filament was not exhibited clearly this case was designated as a moderate interaction. For this, and a few other cases, the categorization of the interactions was difficult. The demarcation lines of Figure 13 are chosen somewhat arbitrarily and are useful simply as a guideline to delineate the flow behavior.

The waves used herein are similar in amplitude but shorter in wavelength to those in Sveen *et al.*[24]. The descriptions of the wave-hill interactions have also been quite similar. This, in addition to the upper layer being unaffected mostly by the wave-hill interaction indicates that the interaction is independent of mode number. The lower half of the mode-2 ISW (that which is below the pycnocline centre) is the effective region of influence. Since this region appears approximately as a mode-1 ISW of depression with an upper boundary at the pycnocline centre, the similarity between the different modes is unsurprising. The wave

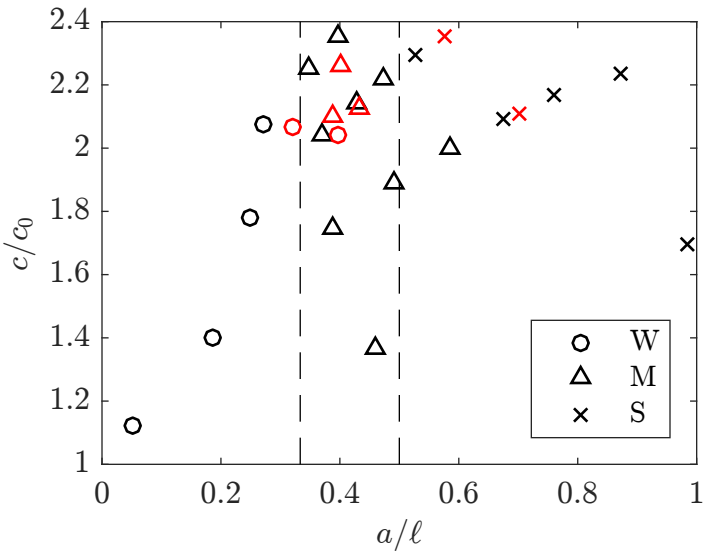

FIG. 13. Non-dimensional wave speed versus non-dimensional amplitude. Black (red) markers correspond to simulations (experiments). The legend indicates the wave-hill interaction type. Vertical dashed lines are where $a/\ell = 1/3$ and $a/\ell = 1/2$.

structure, particularly the wavelengths, are different between the modes so the interactions are not exactly comparable.

VII. SUMMARY

We have conducted numerical and physical experiments of mode-2 ISWs traversing an isolated ridge. We have focused on a particularly narrow topography, while adjusting the size of the wave and the depth of the fluid. The wave amplitudes compared with the pycnocline half-width were in the range 0.21-3.56, putting them in the highly non-linear regime. When compared with the minimum lower layer depth the amplitude was in the range 0.05-1.5; most cases where less than unity.

We have found that the wave-hill interaction can be broken down into three regimes: weak, moderate, and strong interactions. The first occurs when the wave amplitude non-dimensionalized by the minimum lower layer depth, a/ℓ, is less than about 1/3. The second, moderate interaction, occurs where the wave induces vorticity in the boundary layer of the hill, but is itself left largely unaffected. The third, when $a/\ell > 1/2$, has powerful vorticity generated at the hill crest and core material is extracted from the wave in the form of a thin

filament of core fluid.

The moderate and strong interaction types result in the transport of material from the surface of the topography and the BBL into the water column. Rapid resuspension was coupled with a strong vortex formed during the filamentary extraction of core fluid in the strong interaction case. Moderate interactions contained weaker, yet persistent vorticity which over time pumped BBL material into the water column. It is hard to over-emphasize the ease in which vorticity is produced and its role in resuspending material.

The greatest surface stress coincided with the generation of vorticity. In strong interactions this occurred just prior to the formation of the filament. The loss of core material in strong interactions led to a readjustment of the wave, while inducing density overturning above the hill. In moderate and weak interaction the wave was only slightly modulated even though the fluid depth changed a significant amount (at a minimum being reduced by 25%, and at a maximum being reduced by 40%). Waves that experience these weaker interactions may therefore repeatedly interact with a sequence of ridges.

The wave-hill interaction was quick (approximately 30 non-dimensional time units) in all cases. At most, the mode-2 ISW lost approximately 24% of core material in the formation of the filament. Although this particular interaction was strong, minimal generation of trailing mode-1 waves occurred. That said, in both moderate and strong interactions cases, a small amplitude, trailing mode-1 wavetrain was still visible. In numerical simulations, moderate and strong interaction cases also showed the generation of a leading, long mode-1 ISW that was not detected in the experiments because of the small amplitude.

While the primary mechanism for vortex generation in the strong breaking cases was the same for a variety of Reynolds numbers, the fine-scale structure increased with Reynolds number. Since observations of mode-2 ISWs typically have higher Reynolds numbers than those used here-within, the vortex generation and wave breaking might be more effective at inducing turbulent mixing.

Resuspension associated with wave breaking in both mode-1 and mode-2 ISWs has now been documented by multiple studies at the experimental scale. It is now important that field scale observations be made to accurately measure the applicability of these idealized studies to a more dynamic and chaotic natural environment. Future numerical modeling work could simulate oceanic conditions similar to those experienced by mode-2 waves in the Heng-Chun Ridge area[4], though the wide discrepancy in scales between the waves and

the boundary layer in the field will prove a challenge for numerical methods. More realistic representations of sediment, including some form of settling velocity and a Shields-type criterion for resuspension would also add to the applicability of future simulations, and allow for studies of not only particle resuspension but subsequent settling out and redistribution due to shoaling ISWs.

VIII. SUPPLEMENTARY MATERIAL

Figures 3, 4, 6, and the right column of Figure 7 have corresponding videos presenting the time lapse of the interaction between the wave and the ridge for the numerical density field (Figures 3 and 6, for the moderate and strong cases, respectively) and the raw, experimental, false colour image (Figures 4 and 7, for the moderate and strong cases, respectively).

ACKNOWLEDGMENTS

This research was supported by the Natural Sciences and Engineering Research Council of Canada through a Discovery Grant (MS), and the Government of Ontario through a Queen Elizabeth II Graduate Scholarship in Science and Technology (DD). The experimental work was conducted at The University of Dundee by DD and MC with the aid of grants provided by The University of Dundee, the University of St Andrews, and the University of Waterloo. Much appreciation is reserved for the technical assistance provided by John Anderson and David Turbyne. The authors would also like to acknowledge the helpful feedback given by two anonymous referees.

REFERENCES

[1]K. R. Helfrich and W. K. Melville, "Long nonlinear internal waves," Annual Review of Fluid Mechanics **38**, 395–425 (2006).

[2]L. A. Ostrovsky and Y. A. Stepanyants, "Do internal solitions exist in the ocean?" Reviews of Geophysics **27**, 293–310 (1989).

[3]S. R. Ramp, Y. J. Yang, D. B. Reeder, and F. L. Bahr, "Observations of a mode-2 nonlinear internal wave on the northern Heng-Chun Ridge south of Taiwan," Journal of Geophysical Research: Oceans **117** (2012), 10.1029/2011JC007662.

[4]S. R. Ramp, Y. J. Yang, D. B. Reeder, M. C. Buijsman, and F. L. Bahr, "The evolution of mode-2 nonlinear internal waves over the northern Heng-Chun Ridge south of Taiwan," Nonlinear Processes in Geophysics Discussions **2**, 243–296 (2015).

[5]J. da Silva, M. Buijsman, and J. Magalhaes, "Internal waves on the upstream side of a large sill of the Mascarene Ridge: a comprehensive view of their generation mechanisms and evolution," Deep Sea Research Part I: Oceanographic Research Papers **99**, 87–104 (2015).

[6]E. L. Shroyer, J. N. Moum, and J. D. Nash, "Mode 2 waves on the continental shelf: Ephemeral components of the nonlinear internal wavefield," Journal of Geophysical Research **115** (2010), 10.1029/2009jc005605.

[7]Y. J. Yang, Y. C. Fang, T. Y. Tang, and S. R. Ramp, "Convex and concave types of second baroclinic mode internal solitary waves," Nonlinear Processes in Geophysics **17**, 605–614 (2010).

[8]D. Dong, X. Yang, X. Li, and Z. Li, "SAR observation of eddy-induced mode-2 internal solitary waves in the South China Sea," IEEE Transactions on Geoscience and Remote Sensing **54**, 6674–6686 (2016).

[9]A. Brandt and K. R. Shipley, "Laboratory experiments on mass transport by large amplitude mode-2 internal solitary waves," Physics of Fluids **26**, 046601 (2014).

[10]R. E. Davis and A. Acrivos, "Solitary internal waves in deep water," J. Fluid Mech. **29**, 593 (1967).

[11]D. E. Terez and O. M. Knio, "Numerical simulations of large-amplitude internal solitary waves," Journal of Fluid Mechanics **362**, 53–82 (1998).

[12]B. R. Sutherland, "Interfacial gravity currents. I. Mixing and entrainment," Physics of Fluids **14**, 2244–2254 (2002).

[13]A. P. Mehta, B. R. Sutherland, and P. J. Kyba, "Interfacial gravity currents. II. Wave excitation," Physics of Fluids **14**, 3558–3569 (2002).

[14]M. Salloum, O. M. Knio, and A. Brandt, "Numerical simulation of mass transport in internal solitary waves," Physics of Fluids **24**, 016602 (2012).

[15]A. P. Stamp and M. Jacka, "Deep-water internal solitary waves," Journal of Fluid Mechanics **305**, 347–371 (1995).

[16]T. B. Benjamin, "Internal waves of permanent form in fluids of great depth," J. Fluid Mech. **29**, 559 (1967).

[17]D. Deepwell and M. Stastna, "Mass transport by mode-2 internal solitary-like waves," Physics of Fluids **28**, 056606 (2016).

[18]M. Carr, P. A. Davies, and R. P. Hoebers, "Experiments on the structure and stability of mode-2 internal solitary-like waves propagating on an offset pycnocline," Physics of Fluids **27**, 046602 (2015).

[19]J. Olsthoorn, A. Baglaenko, and M. Stastna, "Analysis of asymmetries in propagating mode-2 waves," Nonlinear Processes in Geophysics **20**, 59–69 (2013).

[20]K. Terletska, K. T. Jung, T. Talipova, V. Maderich, I. Brovchenko, and R. Grimshaw, "Internal breather-like wave generation by the second mode solitary wave interaction with a step," Physics of Fluids **28**, 116602 (2016).

[21]A. S. Belogortsev, S. A. Rybak, and A. N. Serebryanyi, "Second-mode nonlinear internal waves over a sloping bottom," Acoustical Physics **59**, 62–67 (2013).

[22]K. G. Lamb and W. Xiao, "Internal solitary waves shoaling onto a shelf: Comparisons of weakly-nonlinear and fully nonlinear models for hyperbolic-tangent stratifications," Ocean Modelling **78**, 17–34 (2014).

[23]M.-H. Cheng, J. R.-C. Hsu, and C.-Y. Chen, "Laboratory experiments on waveform inversion of an internal solitary wave over a slope-shelf," Environmental Fluid Mechanics **11**, 353–384 (2011).

[24]J. K. Sveen, Y. Guo, P. A. Davies, and J. Grue, "On the breaking of internal solitary waves at a ridge," Journal of Fluid Mechanics **469**, 161–188 (2002).

[25]Y. Guo, J. K. Sveen, P. A. Davies, J. Grue, and P. Dong, "Modelling the motion of an internal solitary wave over a bottom ridge in a stratified fluid," Environmental Fluid Mechanics **4**, 415–441 (2004).

[26]E. L. Hult, C. D. Troy, and J. R. Koseff, "The breaking of interfacial waves at a submerged bathymetric ridge," Journal of Fluid Mechanics **637**, 45 (2009).

[27]E. L. Hult, C. D. Troy, and J. R. Koseff, "The mixing efficiency of interfacial waves breaking at a ridge: 1. Overall mixing efficiency," Journal of Geophysical Research **116** (2011), 10.1029/2010jc006485.

[28]E. L. Hult, C. D. Troy, and J. R. Koseff, "The mixing efficiency of interfacial waves breaking at a ridge: 2. Local mixing processes," Journal of Geophysical Research **116** (2011), 10.1029/2010jc006488.

[29]H. Zhu, L. Wang, E. Avital, H. Tang, and J. Williams, "Numerical simulation of interaction between internal solitary waves and submerged ridges," Applied Ocean Research **58**, 118–134 (2016).

[30]T. Maxworthy, "On the formation of nonlinear internal waves from the gravitational collapse of mixed regions in two and three dimensions," Journal of Fluid Mechanics **96**, 47–64 (1980).

[31]V. Maderich, T. Talipova, R. Grimshaw, K. Terletska, I. Brovchenko, E. Pelinovsky, and B. H. Choi, "Interaction of a large amplitude interfacial solitary wave of depression with a bottom step," Physics of Fluids **22**, 076602 (2010).

[32]T. Talipova, K. Terletska, V. Maderich, I. Brovchenko, K. T. Jung, E. Pelinovsky, and R. Grimshaw, "Internal solitary wave transformation over a bottom step: Loss of energy," Physics of Fluids **25**, 032110 (2013).

[33]P. K. Kundu, I. M. Cohen, and D. R. Dowling, *Fluid Mechanics*, 5th ed. (Academic Press, 2012).

[34]C. J. Subich, K. G. Lamb, and M. Stastna, "Simulation of the Navier-Stokes equations in three dimensions with a spectral collocation method," Int. J. Num. Meth. Fluids **73**, 103–129 (2013).

[35]P. A. Davies, "Aspects of flow visualisation and density field monitoring of stratified flows," Optics and Lasers in Engineering **16**, 311–335 (1992).

[36]S. B. Dalziel, M. Carr, J. K. Sveen, and P. A. Davies, "Simultaneous synthetic schlieren and PIV measurements for internal solitary waves," Measurement Science and Technology **18**, 533 (2007).

[37]This colormap and the one used in Figure 10 (and other figures like it) were provided by Thyng *et al.*[40].

[38]S. Harnanan, N. Soontiens, and M. Stastna, "Internal wave boundary layer interaction: A novel instability over broad topography," Physics of Fluids **27**, 016605 (2015).

[39]J. Olsthoorn and M. Stastna, "Numerical investigation of internal wave-induced sediment motion: Resuspension versus entrainment," Geophysical Research Letters **41**, 2876–2882 (2014).

[40]K. M. Thyng, C. A. Greene, R. D. Hetland, H. M. Zimmerle, and S. F. DiMarco, "True colors of oceanography: Guidelines for effective and accurate colormap selection," Oceanography **29**, 9–13 (2016).